Supporting Information

In situ observation of sodium dendrite growth and concurrent mechanical property measurements using an ETEM-AFM platform

Qiunan Liu,[1] Liqiang Zhang,[1] Haiming Sun,[1] Lin Geng,[1] Yanshuai Li,[1] Yushu Tang,[4] Peng Jia,[1] Zaifa Wang,[1] Qiushi Dai,[1] Tongde Shen,[1] Yongfu Tang[1,3]*, Ting Zhu[5], and Jianyu* Huang[1,2]*

[1]*Clean Nano Energy Center, State Key Laboratory of Metastable Materials Science and Technology, Yanshan University, Qinhuangdao 066004, P. R. China.*

[2]*School of Materials Science and Engineering, Xiangtan University, Xiangtan, Hunan 411105, P. R. China.*

[3]*Hebei Key Laboratory of Applied Chemistry, College of Environmental and Chemical Engineering, Yanshan University, Qinhuangdao 066004, P.R. China.*

[4]*Institute of Nanotechnology (INT), Karlsruhe Institute of Technology (KIT), Hermann-von-Helmholtz-Platz 1, 76344, Eggenstein-Leopoldshafen, Germany.*

[5]*Woodruff School of Mechanical Engineering, Georgia Institute of Technology, Atlanta, GA 30332, USA*

Corresponding Author

[*]Correspondence to: liqiangzhang85@163.com; tangyongfu@ysu.edu.cn; jhuang8@hotmail.com

Table of Contents

Supplementary Methods

In situ ETEM-AFM

Synthesis of arc discharged CNTs

Effects of surface Na_2CO_3 layer on the mechanical properties of Na dendrites

Molar volume calculation of Li and Na

Quantification of bending off the image plane

Supplementary Movies S1-S21

Supplementary Figures S1-S12

Supplementary Tables S1-S3

REFERENCES

Supplementary Methods

In situ ETEM-AFM

For quantitatively measuring the mechanical strength of the Na dendrite, we developed an ETEM-AFM device for characterization the mechanical properties of Na dendrites. As the deflection of the cantilever (< 1 μm) was much smaller than its beam length (520 μm), a linear relationship between ΔX (displacement of the AFM tip is equal to the cantilever deflection) and F (force applied on the dendrite) was assumed. During the experiment, a beam blocking bar was inserted into the field of view as the reference for displacement measurements. The compression or tensile strengths of Na dendrite was calculated by measuring cantilever deflections in high magnification TEM images.

In the experiment, we first welded a short CNT onto the AFM tip by ebeam induced carbon deposition. After that, the AFM tip and metal Na electrodes were mounted into a TEM-STM (Scanning Tunneling Microscopy) holder (Pico Femto FE-F20) inside a glove box. Then the holder was sealed in a home-built air-tight bag filled with dry argon and transferred to the ETEM. The total time of air exposure was less than 2 s, which limited the extent of oxidization layer formation on the surface of the metal Na. When the CNT and metal Na were connected, an external bias (-2 ~ -8V) was supplied for generating Na dendrites. The voltage was precisely controlled by a potentiostat (PiciFemto V3ST, produced by Anhui Zeyou Technology Co., Ltd.). As a voltage is applied, the current passing through the sample can be characterized at the same time. The variation of measured current is within about ± 0.3 pA. The voltage applied to the sample is the output voltage of the controller, that is, the programming voltage, and the error bar of the voltage is within ± 4.5 mV.

All the dendrite growth and mechanical tests were performed in a CO_2 ambient with a CO_2 gas pressure of 1 mbar.

The AFM sensors were purchased from Burker Company with the stiffness of the AFM cantilever specified by the manufacture. To determine the accuracy of our measurement system, we have conducted additional benchmark experiments. That is, we measured the mechanical strength of five individual single-crystal Ag pillars with our ETEM-AFM system, and then tested another batch of five similar single-crystal Ag pillars with a commercial TEM sample holder (Hysitron PI 95) for mechanical testing. The average of measured yield strengths is $\sigma_{\text{y ETEM-AFM}}$ =

366.0 ± 41.4 MPa from our ETEM-AFM platform, while $\sigma_{y\,PI\,95}$ = 349.2 ± 44.3 MPa from Hysitron PI 95 holder. The difference is about 4.6%, which provides a quantitative measure on the accuracy of our testing system. This information has been provided in our previous paper.[1]

Synthesis of arc discharged CNTs

The CNTs applied in this study were prepared by an electrical arcing method. The anode was an asphalt-derived carbon rod, and the cathode was a high-purity graphite electrode. In order to facilitate the collection of CNTs and improve the purity of the CNT samples, we placed a wire net on the top of the two electrodes in the chamber, and the distance between the wire net and the electrodes was about 5 cm. The buffer gas pressure was controlled in the 0.04-0.05 MPa range during the arc discharge experiment. The DC voltage and current for arcing were controlled at 18-20 V and 60-80 A, respectively. The distance between the two electrodes was maintained at about 1-3 mm by manually advancing the anode that was consumed during the experiment.

Effects of surface Na_2CO_3 layer on the mechanical properties of Na dendrites

In our experiment, a thin layer of Na_2CO_3 formed on the surface of the Na dendrite once CO_2 gas was introduced into the ETEM chamber. The Na_2CO_3 formation was attributed to a chemical reaction between Na and CO_2 via: $Na + CO_2 \rightarrow Na_2CO_3 + C$ or CO. The formation of Na_2CO_3 layer on the surface of the Na dendrites is similar to the formation of a solid electrolyte interface (SEI) layer in the anode in a sodium ion battery (SIB) or sodium metal battery (SMB).

The notion of "smaller is stronger"[2] is well established in conventional metallic materials such as Cu. The yield strength of bulk Cu is less than 100 MPa, however, that of Cu whisker reaches a few GPa, approaching the theoretical strength of Cu.[3] The "smaller is stronger" phenomenon has been recently demonstrated by micron-sized Li pillars,[4] submicron Li whiskers,[1, 5] Li spheres,[6] and even in bulk Li with different length scales.[7] The yield strength of bulk Li is ~1 MPa,[7-10] but that of a micron-sized Li pillar attained over 100 MPa,[4] and that of a nano-sized Li whisker reached over 200 MPa.[1, 5] Therefore the observed high strength of Na dendrites with a surface Na_2CO_3 layer is consistent with the trend of Li, which is a similar type of alkali metal as Na.

It is still a significant challenge to quantitatively evaluate the effects of the Na_2CO_3 surface layer at this stage. However, the tensile experiment shown in Figure 6 is a good example that illustrates how the Na_2CO_3 surface layer affects mechanical measurements. As we imposed a large tensile

displacement to a single Na dendrite, the Na_2CO_3 surface layer became much thinner in the central elongated part of this dendrite, and eventually becomes nearly invisible (Figure 6b-e). This suggests a loss of mechanical constraints of the Na_2CO_3 surface layer on the Na dendrite, resulting from a large plastic stretch or possible damage/fracture of Na_2CO_3. Nevertheless, the measured yield strengths are still very high. Therefore, this result provides strong evidence that the observed high yield strength can be mainly attributed to the intrinsic size effect. We also note that the Na_2CO_3 surface layer of nanometer thick has the structure in between a nanocrystalline and amorphous state, which is less dense than its bulk counterpart. As a result, this nanolayer is likely much softer elastically and/or plastically, thus imposing less mechanical constraints on the overall elastic-plastic responses of Na dendrites. Nonetheless, the impact of Na_2CO_3 surface layers on the measured mechanical strengths may not be negligible and warrant in-depth studies in the future.

Molar volume calculation of Li and Na

From the Periodic Table, the molar masses for Li and Na are: m_{Li} = 6.9 g mol^{-1} and m_{Na} = 22.99 g mol^{-1}, respectively. The densities for Li and Na are: ρ_{Li} = 0.53 g cm^{-3} and ρ_{Na} = 0.97 g cm^{-3},[11] respectively. The molar volumes of Li and Na are then: $V_{Li} = m_{Li}/\rho_{Li}$ = 13.02 cm^3 mol^{-1} and $V_{Na} = m_{Na}/\rho_{Na}$ = 23.70 cm^3 mol^{-1}, respectively. It can be seen that the calculated molar volume for Li agrees very well with that from ref.[12]

Quantification of bending off the image plane

To observe the deformation of a Na dendrite in a TEM, the imaging condition has to be adjusted to focus on the image plane when needed. Once a segment of the dendrite (usually near the AFM tip) bends off the image plane, the image of that segment becomes blurred. Therefore one has to change the image focus in order to see the bent segment clearly. We deemed that bending occurred once the image was blurred. From the changes of focus, one can estimate the bending deformation. For example, the image magnification in Figure 4c is ×13,000, and the focus step is about 3 nm; by counting the number of turns made to the focus knob in order to bring the blurred image into focus, one can obtain a rough estimate of the magnitude of bending deformation.

Supplementary Movies

Description of Movie S1

An *in situ* TEM movie showing the growth of a Na dendrite (**Figure 1**). The Na dendrite grew directly along the CNT. The movie was recorded at 5 frames/second in TEM bright field images, and played at 84× speed.

Description of Movie S2

An *in situ* TEM movie showing the growth of a Na dendrite (**Figure 2a-e**). The movie was recorded at 5 frames/second, and played at 338× speed.

Description of Movie S3

An *in situ* TEM movie showing the growth of a Na dendrite under different potentials (**Figure 2m-s**). The movie was recorded at 5 frames/second, and played at 195× speed.

Description of Movie S4

An *in situ* TEM movie showing the growth of a Na dendrite (**Figure 3a-d**). The movie was recorded at 5 frames/second in a TEM bright field mode, and played at 357× speed.

Description of Movie S5

An *in situ* TEM movie showing the growth of a Na dendrite (**Figure 3e-h**). The movie was recorded at 5 frames/second, and played at 40× speed.

Description of Movie S6

An *in situ* TEM movie showing the growth of the Na nanocube (**Figure 3i-l**). The movie was recorded at 5 frames/second, and played at 283× speed.

Description of Movie S7

An *in situ* TEM movie showing the growth of a Na nanorod (**Figure S4a-d**). The movie was recorded at 5 frames/second, and played at 130× speed.

Description of Movie S8

An *in situ* TEM movie showing the growth of a Na nanocube (**Figure S5a-d**). The movie was recorded at 5 frames/second, and played at 337× speed.

Description of Movie S9

Assessing the mechanical properties of a Na dendrite by *in situ* compression (**Figure 4c**). After its growth, the dendrite was pushed up against the AFM cantilever, causing the dendrite to deform. The movie was recorded at 5 frames/second, and played at 32× speed.

Description of Movie S10

Measuring the mechanical properties of a Na nanoparticle by *in situ* compression (**Figure 5a**). After its growth, the nanoparticle was pushed up against the AFM cantilever, causing the nanoparticle to deform. The movie was recorded at 5 frames/second, and played at 31× speed.

Description of Movie S11

Assessing the mechanical properties of a Na dendrite by *in situ* tensile test (**Figure 6a-d**). After its growth, the dendrite was pulled down, causing the dendrite to deform until breakage. The movie was recorded at 5 frames/second, and played at 8× speed.

Description of Movie S12

Assessing the mechanical properties of a Na nanorod by *in situ* compression (**Figure S7a**). After its growth, the nanorod was pushed up against the AFM cantilever, causing the nanorod to deform. The movie was recorded at 5 frames/second, and played at 12× speed.

Description of Movie S13

Assessing the mechanical properties of a Na nanosphere by *in situ* compression (**Figure S8a-c**). After its growth, the Na nanosphere was pushed up against the AFM cantilever, causing the Na ball to deform. The movie was recorded at 5 frames/second, and played at 14× speed.

Description of Movie S14

Assessing the mechanical properties of a Na nanosphere by *in situ* compression (**Figure S8d-f**).

After its growth, the Na nanosphere was pushed up against the AFM cantilever, causing the Na nanosphere to deform. The movie was recorded at 5 frames/second, and played at 41× speed.

Description of Movie S15

Assessing the mechanical properties of a Na nanosphere by *in situ* tensile deformation (**Figure S9a-d**). After its growth, the Na nanosphere was pulled down, causing the nanosphere to deform until breakage. The movie was recorded at 5 frames/second, and played at 11× speed.

Description of Movie S16

Assessing the mechanical properties of a Na nanosphere by *in situ* tensile deformation (**Figure S9e-h**). After its growth, the Na nanosphere was pulled down, causing the nanosphere to deform until breakage. The movie was recorded at 5 frames/second, and played at 14× speed.

Description of Movie S17

Assessing the mechanical properties of a Na nanorod by *in situ* tensile deformation (**Figure S9i-k**). After its growth, the Na nanorod was pulled down against the AFM cantilever, causing the nanorod to deform until breakage. The movie was recorded at 5 frames/second in bright field mode, and played at 9× speed.

Description of Movie S18

In situ TEM movie showing the growth of a Na_2CO_3 pillar (**Figure 7a-e**). Upon applying a negative potential to the CNT against the Na anode, Na climbed up the CNT, and it turned almost entirely into Na_2CO_3 under ebeam irradiation in a CO_2 ambient. The Na_2CO_3 pillar is strongly tapered with the upper end much thinner than the lower end. The movie was recorded at 5 frames/second, and played at 297× speed.

Description of Movie S19

Assessing the mechanical properties of a Na_2CO_3 pillar (**Figure 7g-j**). The movie was recorded at 5 frames/second, and played at 33× speed. Note that the "larger strain" in the video than that in Figure 7g-j is in fact caused by bending of the pillar and the corresponding stress does not reflect the intrinsic mechanical properties of the material.

Description of Movie S20

Assessing the mechanical properties of another Na_2CO_3 pillar (**Figure 7k-n**). The movie was recorded at 5 frames/second, and played at 13× speed. Note that the "larger strain" in the video than that in Figure 7k-n is in fact caused by bending of the pillar and the corresponding stress does not reflect the intrinsic mechanical properties of the material.

Description of Movie S21

Assessing the mechanical properties of a Na_2CO_3 nanosphere by *in situ* compression (**Figure 8a-d**). After its growth, the Na_2CO_3 nanosphere was pushed up against the AFM cantilever, causing the nanosphere to deform. The movie was recorded at 5 frames/second, and played at 38× speed.

Supplementary Figures

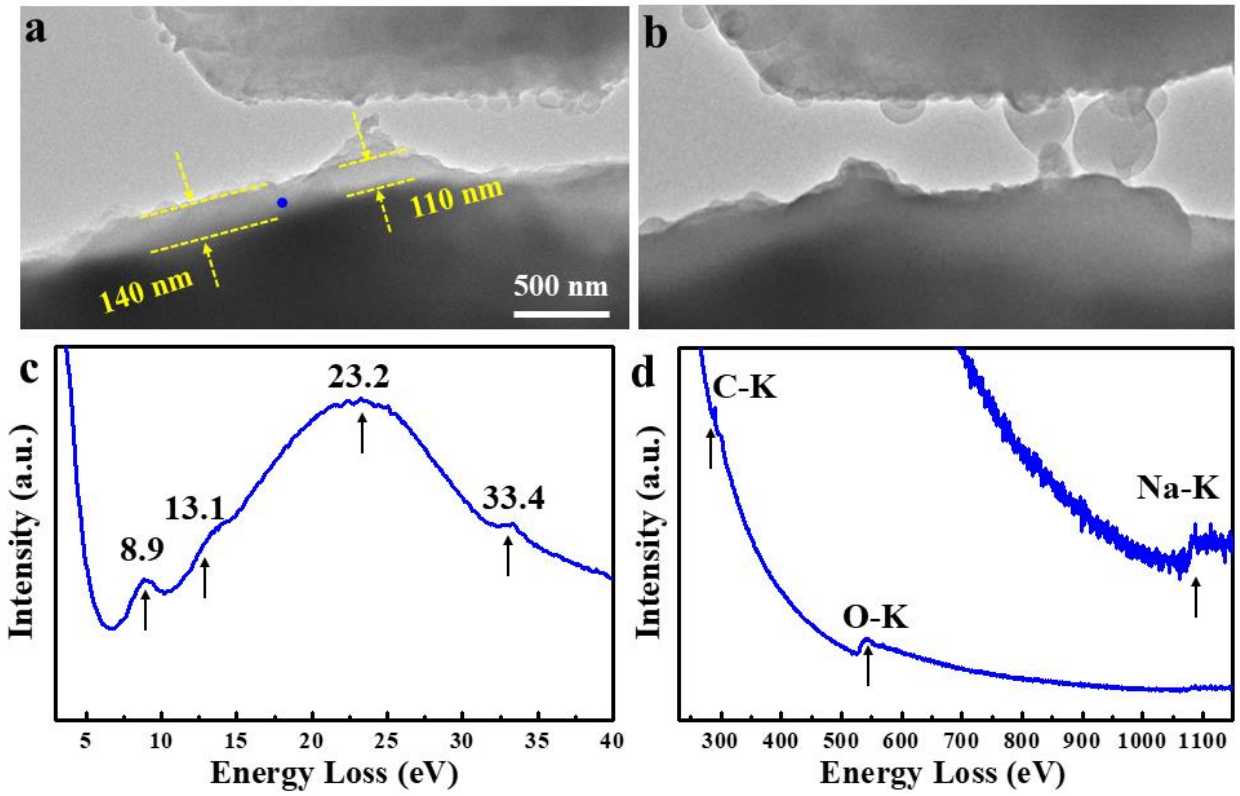

Figure S1. (a) The Na substrate covered by a Na_2CO_3 SEI layer with a thickness of 110 ~ 140 nm. (b) Na nanospheres grown on the Na substrate. A Low-loss (c) and a core-loss (d) electron energy loss spectroscopy (EELS) of the Na substrate.

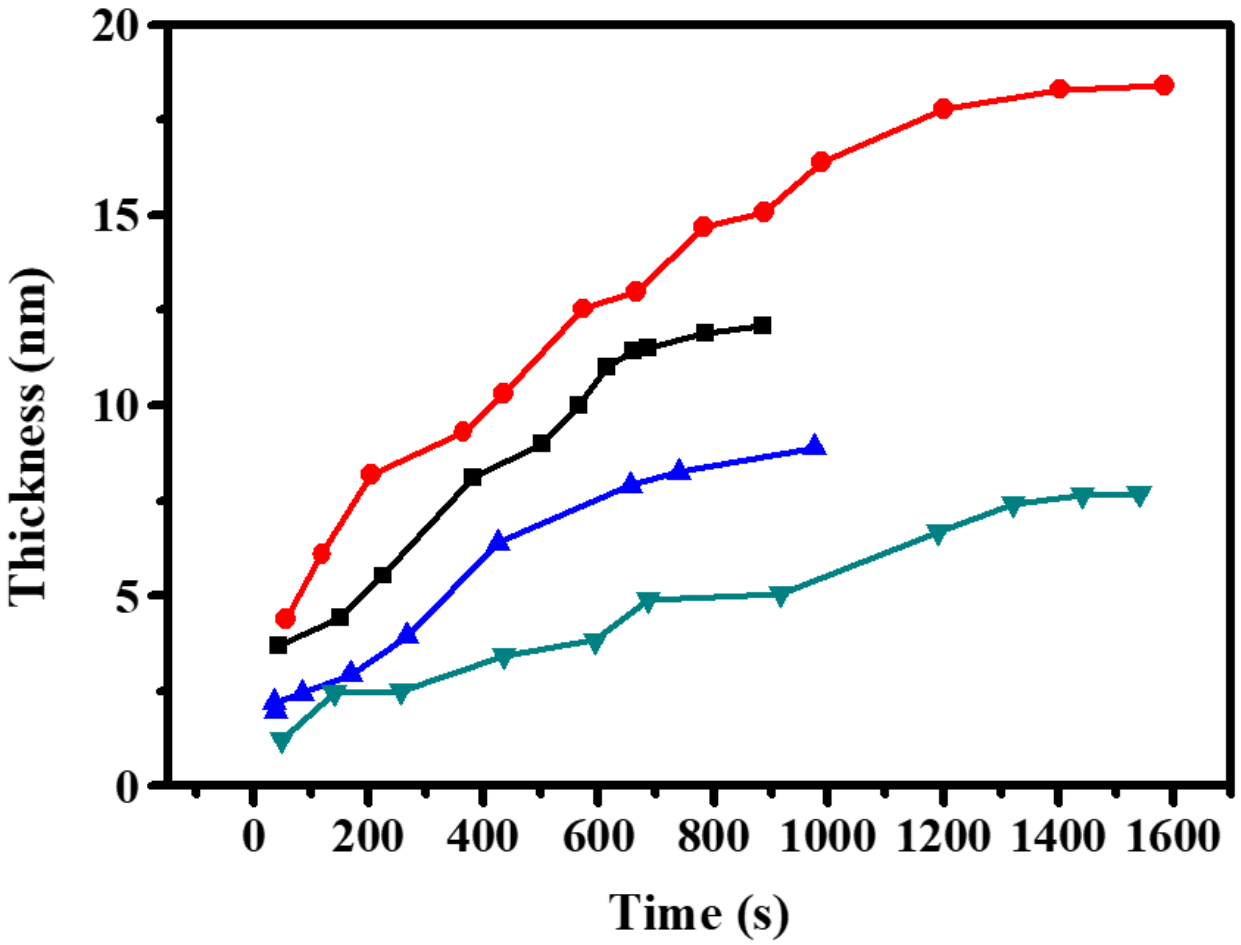

Figure S2. The growth thickness of Na_2CO_3 layer versus time for four typical Na dendrites.

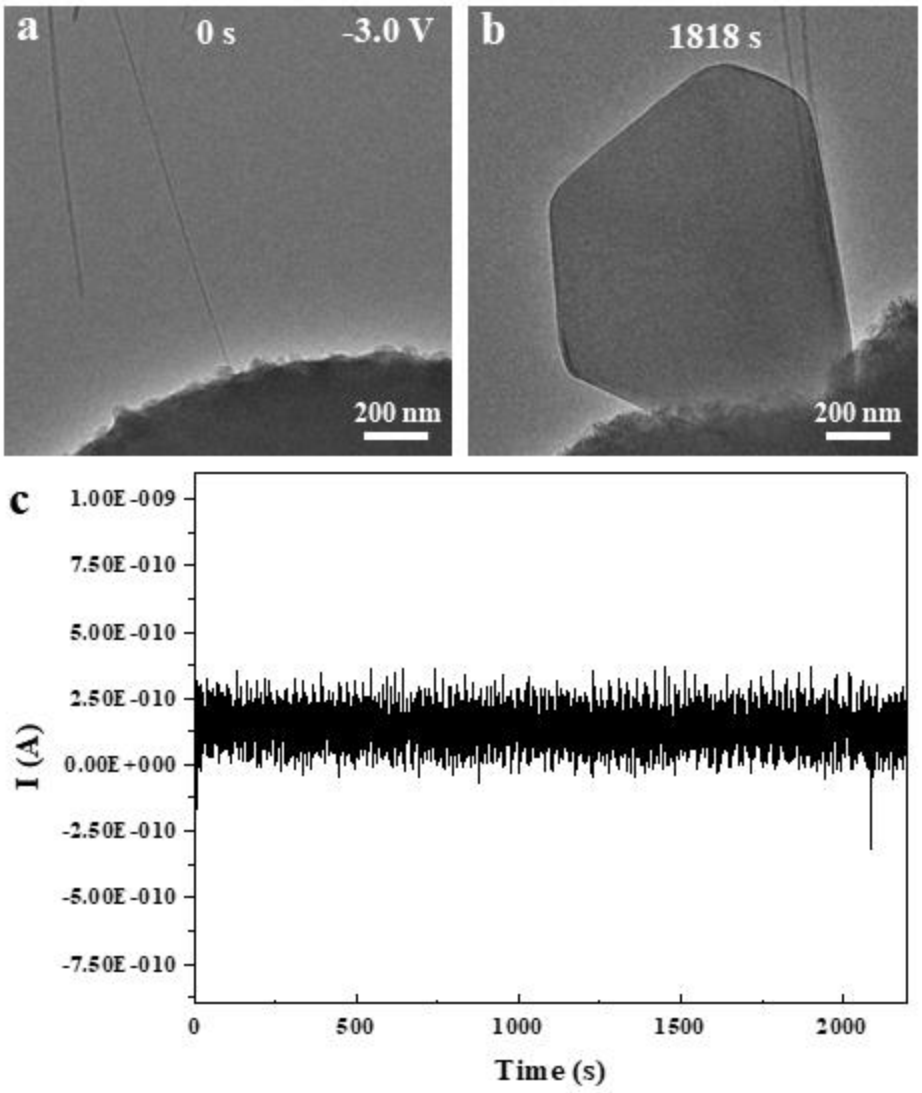

Figure S3. (a-b) *In situ* TEM images of the Na dendrite growth. (c) The current flowing in the dendrite in (a-b).

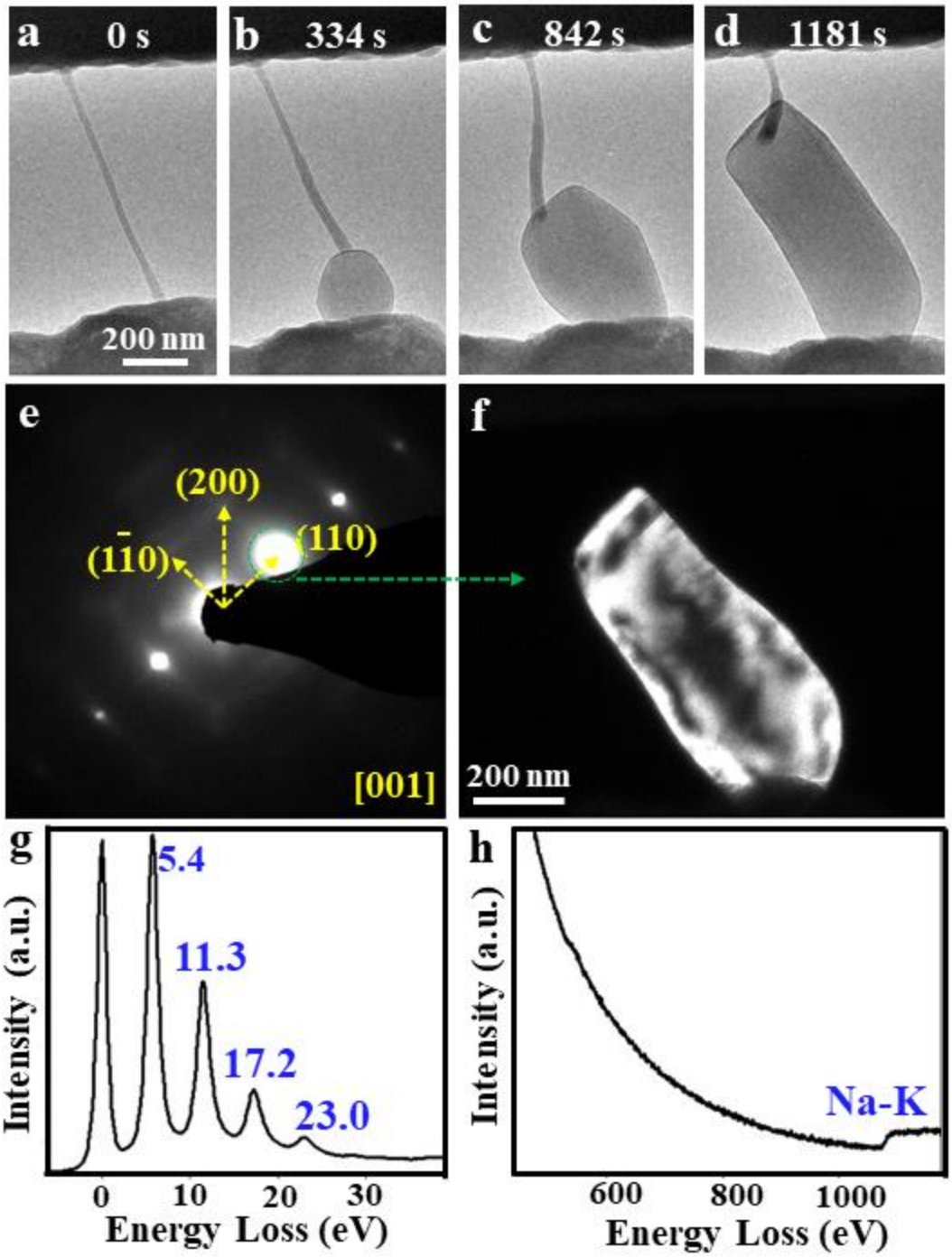

Figure S4. Time lapse TEM images showing the growth of a Na nanorod via electrochemical plating. (a) The initial state, (b) A nanosphere emerged at the CNT, Na_2CO_3 and CO_2 triple point, which was then elongated with a flat top (c), eventually evolved into a dendrite (d). The tip shape of the dendrite remained unchanged during its growth process, implying a root growth mechanism. (e) An EDP of the Na dendrite. (f) A dark field image of the Na dendrite formed by selecting the

(110) reflections in the EDP shown in (e). Low-loss (g) and core-loss (h) EELS showing the characteristics of Na.

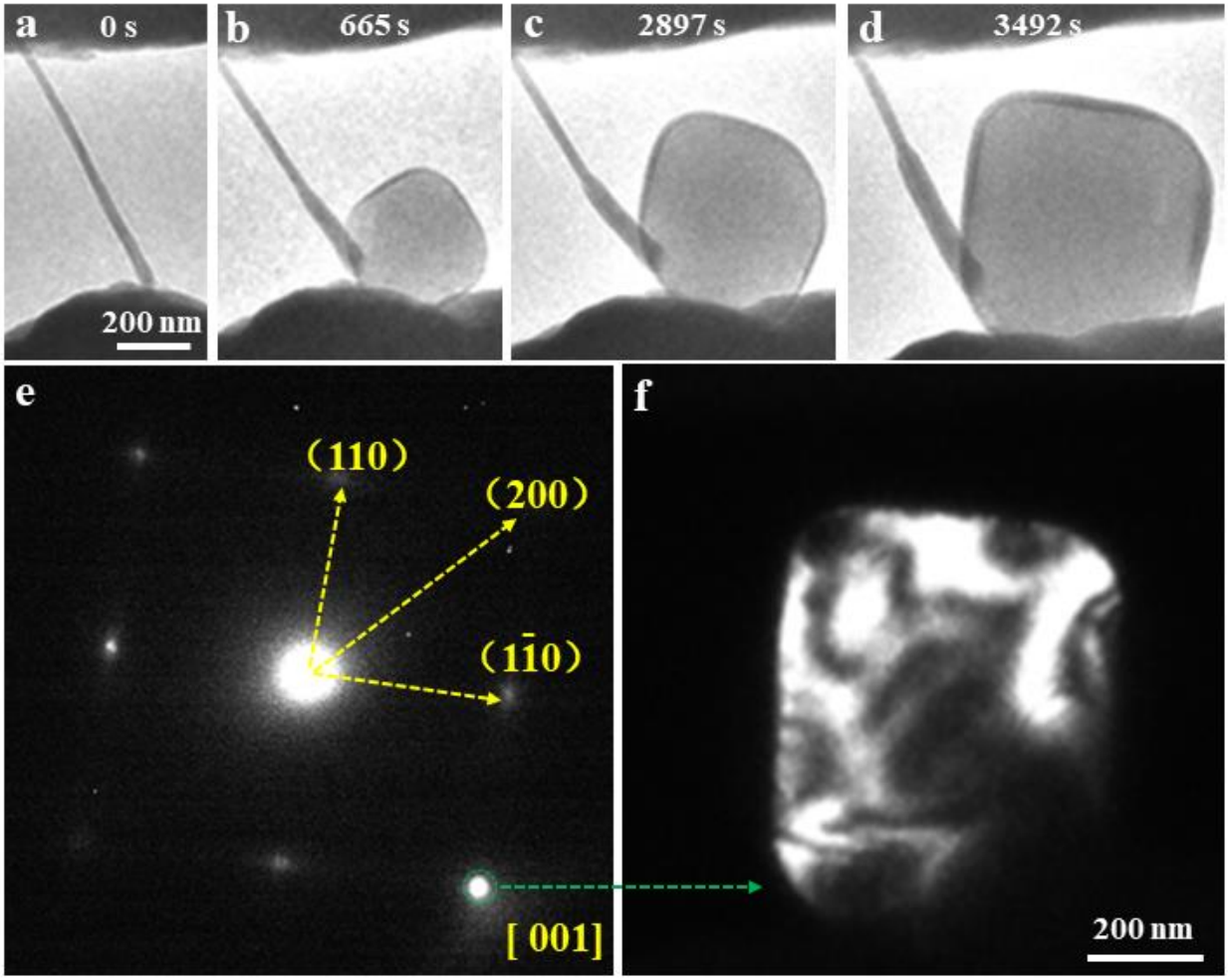

Figure S5. Time lapse TEM images showing the growth of a Na nanocube via electrochemical plating (a-d). (e) An EDP of the Na nanocube. From (f), the nanocube appears to be heavily strained, suggesting there exists significant diffusion induced stress during the growth.

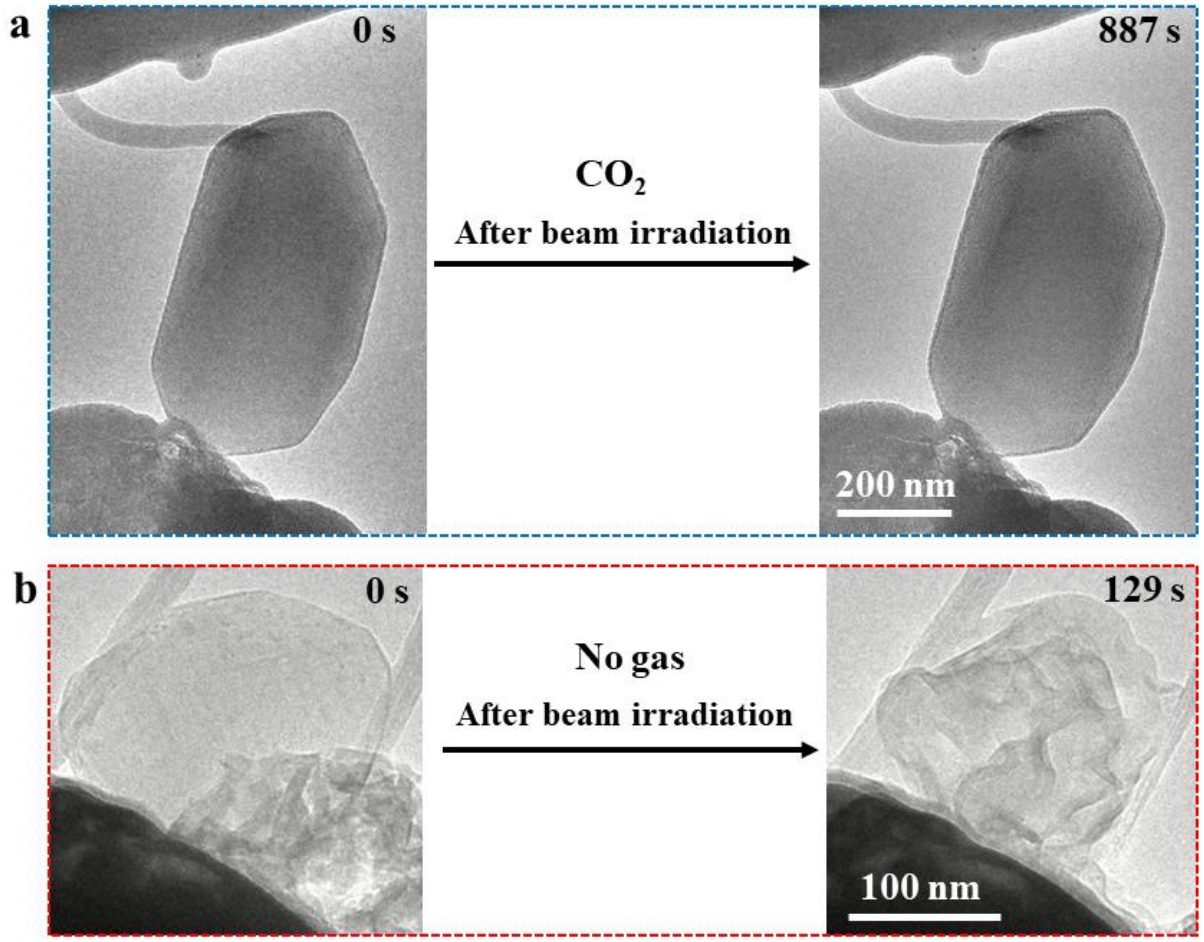

Figure S6. (a) The Na dendrite was exposed to ebeam irradiation for 887 s in a CO_2 ambient, showing no discernible irradiation damage due to the protection of the surface Na_2CO_3 layer. (b) Under no gas condition, the dendrite only grew with a Na plate. The Na plate was quickly broken under beam irradiation for 129 s. The experiment highlights the importance of the CO_2 gas and the formation of the surface Na_2CO_3 layer in facilitating the Na dendrite growth and its subsequent stabilization.

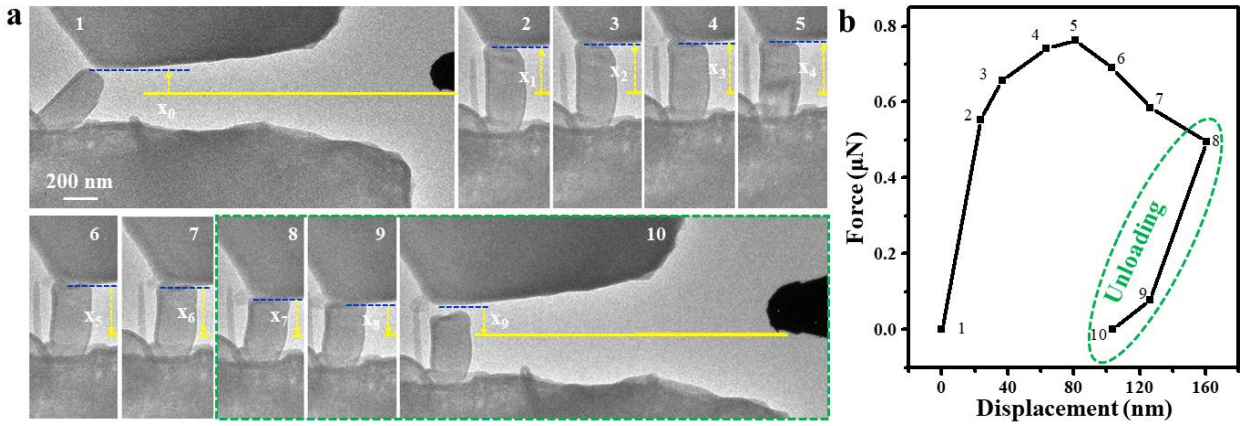

Figure S7. Sequential TEM images showing the compression process (a) and the corresponding force-displacement (b) of a Na nanorod (Corresponding to Movie S12). The Arabic numbers in (a) and (b) have a one-to-one correspondence, meaning that each data point in (b) was measured from the corresponding image shown in (a). The displacement of the AFM cantilever was measured using a beam blocking bar (the dark object on the upper-right corner of frames 1 and 10 in (a)) as a reference. The position of the beam blocking bar remained unchanged during the entire mechanical testing. To save space, the beam blocking bar is not shown in each image, but its position is marked by a solid horizontal yellow line in each frame. The compression strength was measured to be 113 MPa. The spring constant of the Si AFM cantilever beam is k = 6 N m^{-1}. The corresponding mechanical data is shown in Table S2. The stress of the nanorod was calculated by the force divided by the cross-sectional area calculated from the diameter of the nanorod. The thickness of the surface Na_2CO_3 layer is 15 nm.

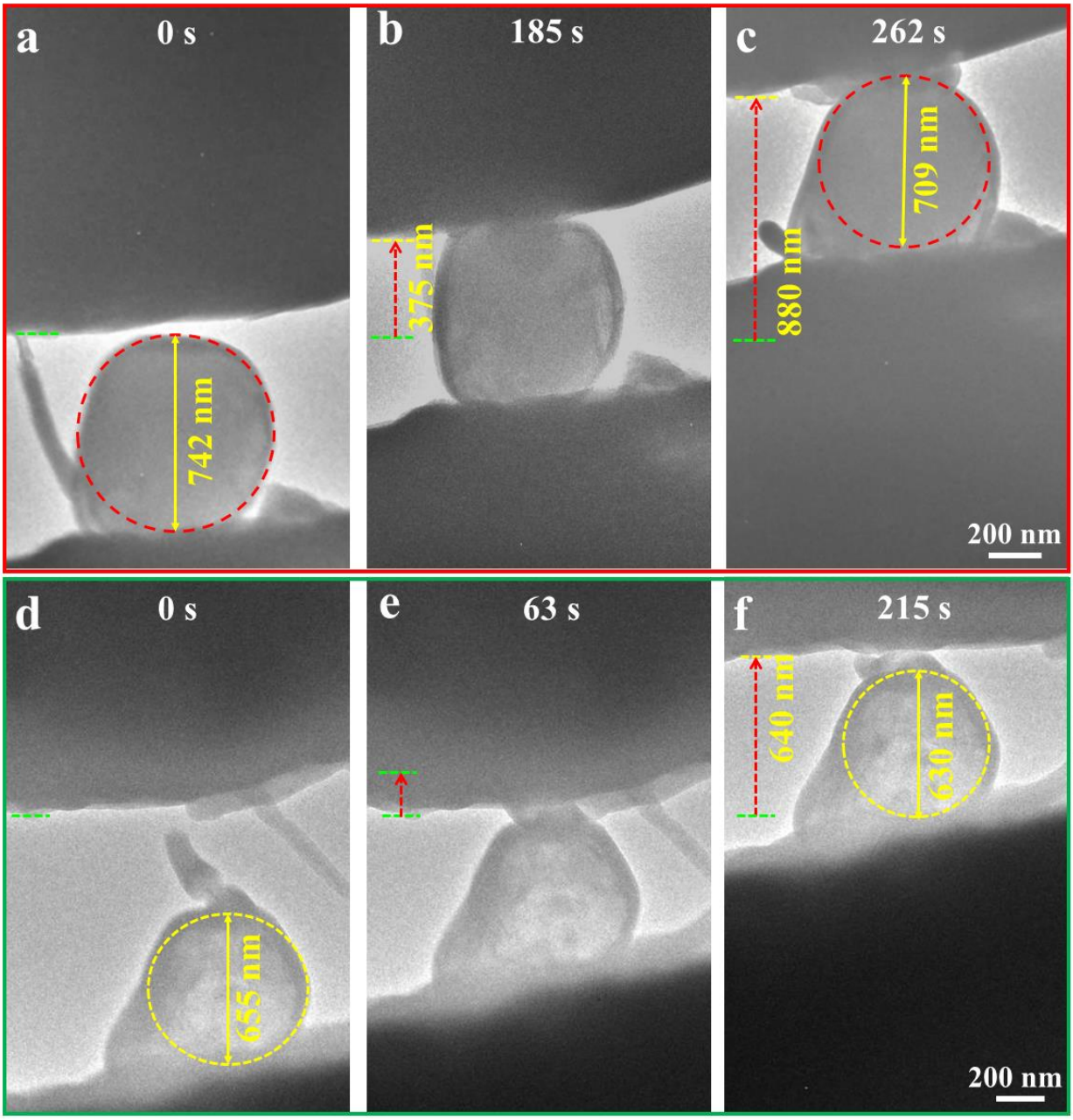

Figure S8. Two sets of *in situ* compression tests of as-grown Na dendrites. The compression strength was measured to be 139 MPa (a-c) and 151 MPa (d-f), respectively. The spring constant of the Si AFM cantilever beam is k = 6 N m^{-1}. The thickness of the surface Na_2CO_3 layer is 19 nm (a-c) and 20 nm (d-f), respectively.

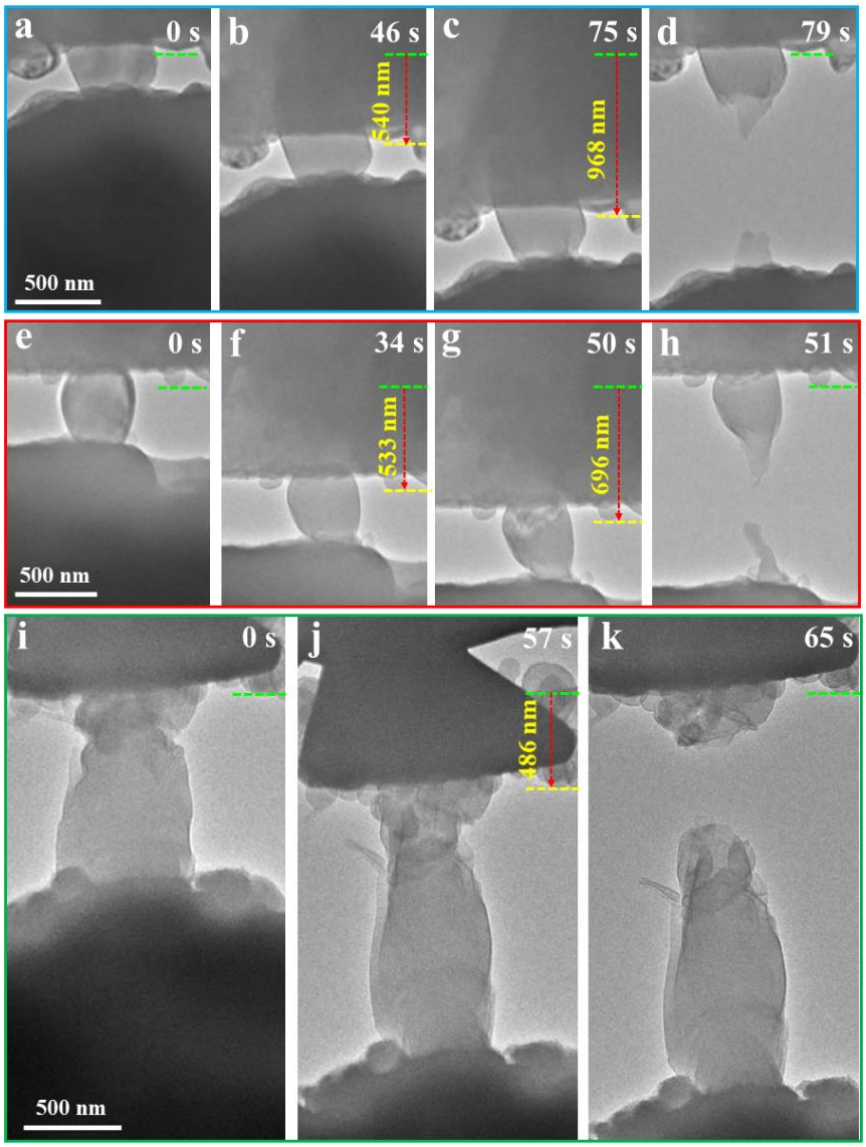

Figure S9. Three sets of *in situ* tensile tests of as-grown Na dendrites. The spring constant of the Si AFM cantilever beam is k = 3 N m^{-1}. Due to the high viscosity of sodium metal, the Na nanosphere and AFM can be well connected after growth, enabling the tensile tests. (a-d) The tensile strength was measured to be 203 MPa. When the displacement of the AFM tip reached about 968 nm, the Na dendrite snapped. The fracture surface exhibits significant necking (d), indicating a ductile fracture characteristic. The corresponding stress-strain curve is shown in Figure 6e (dark line), and the young's modulus is about 2.0 GPa. (e-h) The tensile strength was measured to be 187 MPa. During tension, the dendrite was elongated from near the lower contact (g), and eventually fractured (h). Significant necking occurred before fracture (h). The corresponding stress-strain curve is shown in Figure 6e (red line), and the young's modulus was

measured to be about 3.5 GPa. (i-k) The tensile strength was measured to be 110 MPa. The deformation occurred mainly near the upper contact (j), and significant necking occurred in the fracture surface (k). The thickness of the surface Na_2CO_3 layer is 6 nm (a-d), 8 nm (e-h) and 5 nm (i-k), respectively.

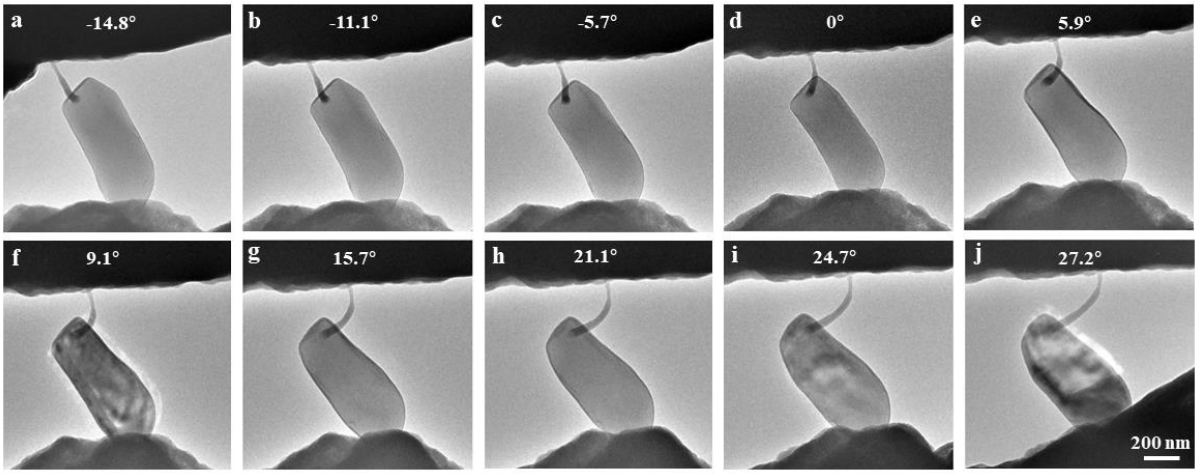

Figure S10. Tilting the as grown Na dendrite from -14.8º to 27.2º.

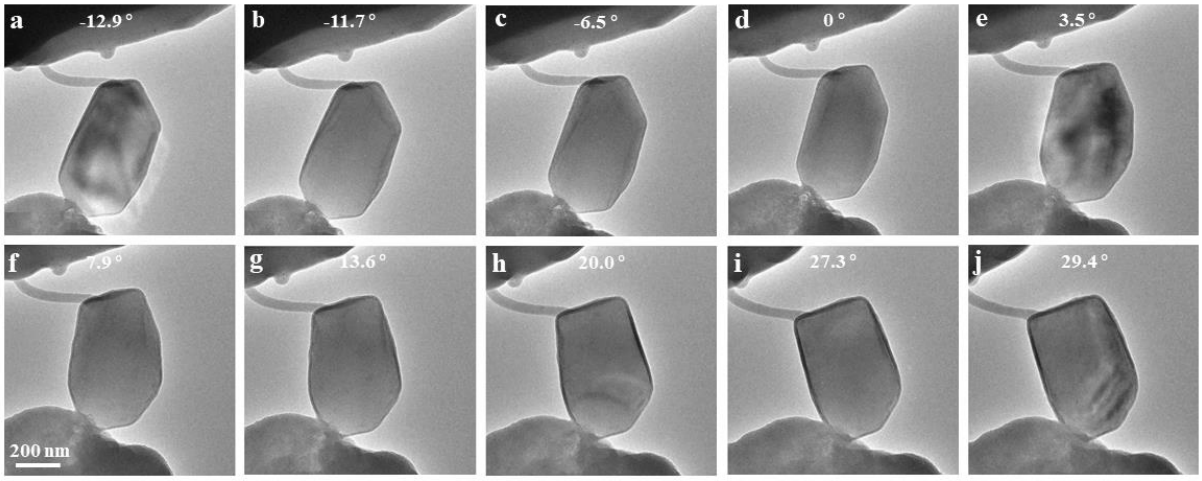

Figure S11. Tilting the as grown Na dendrite from -12.9º to 29.4º.

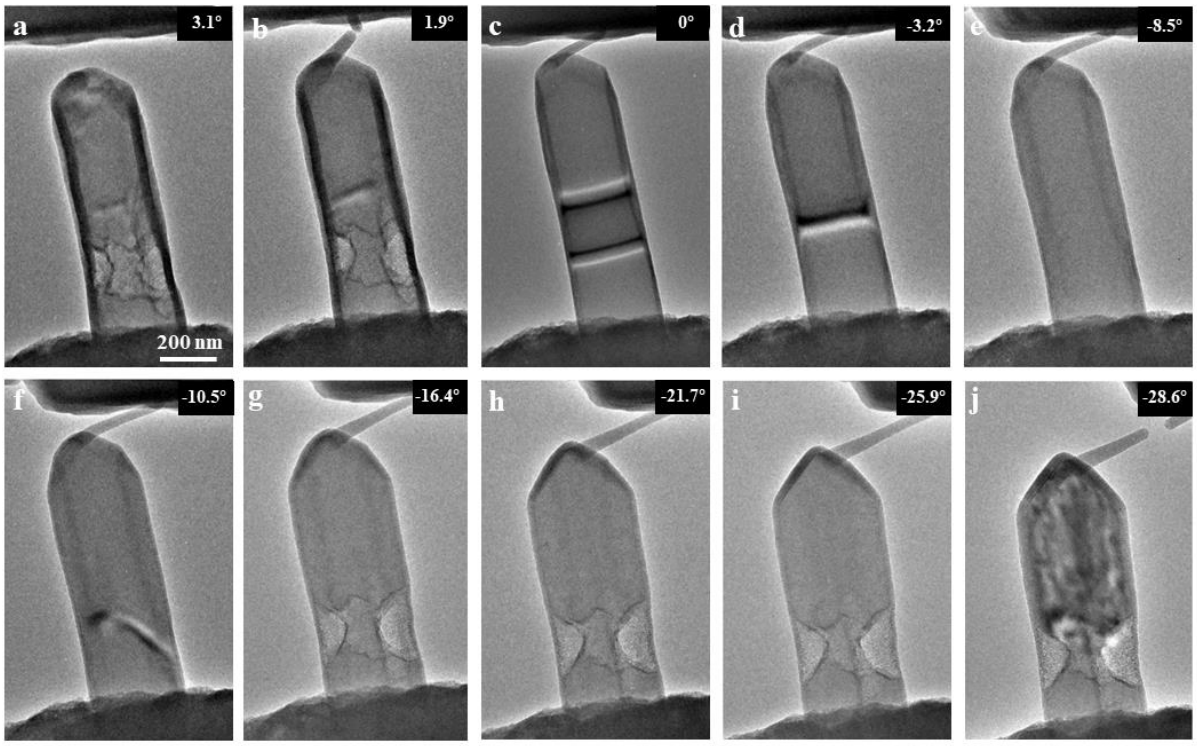

Figure S12. Tilting the as grown Na nanorod from 3.1° to -28.6°.

Supplementary Tables

Table S1. Mechanical data corresponding to Figure 4. D is the height change of the nanorod, and ΔX is the displacement of AFM. F is the force exerted on the Na nanorod.

No.	1	2	3	4	5	6	7	8
F (nN)	0	378.6	723.6	1014.6	1359.0	1999.2	2452.2	2977.2
D (nm)	0	3.3	7.4	8.8	10.7	12.8	14.8	20.1
ΔX (nm)	0	63.1	120.6	169.1	226.5	333.2	408.7	496.2
No.	9	10	11	12	13	14	15	16
F (nN)	3164.4	3338.4	3388.2	3572.4	3594.6	3325.2	3204	3088.2
D (nm)	24.2	30.0	34.4	61.9	65.9	70.3	77.3	83.4
ΔX (nm)	527.4	556.4	564.7	595.4	599.1	554.2	534	514.8
No.	17	18	19	20	21	22	23	24
F (nN)	2911.8	2609.4	2246.4	1644.6	1263.6	456.0	0	-364.8
D (nm)	85.6	72.9	65.9	61.5	54.9	41.8	30.9	19.9
ΔX (nm)	485.3	434.9	347.4	274.1	210.6	76.0	0	-60.8

Table S2. Mechanical data corresponding to Figure S7. D is the height change of the nanorod, and ΔX is the displacement of AFM. F is the force exerted on the Na nanorod.

No.	1	2	3	4	5	6	7	8
F (nN)	0	553.8	657.0	740.4	762.6	689.4	584.4	496.2
D (nm)	0	23.5	36.6	63.4	81	103.3	126.5	160.4
ΔX (nm)	0	92.3	109.5	123.4	127.1	114.9	97.4	82.7
No.	9	10						
F (nN)	77.4	0						
D (nm)	126.3	103.7						
ΔX (nm)	12.9	0						

Table S3. Mechanical data corresponding to Figure 5. D is the height change of the nanoparticle, and ΔX is the displacement of AFM. F is the force exerted on the Na nanoparticle.

No.	1	2	3	4	5	6	7	8
F (nN)	0	373.2	1092	2448	2724	3054	3816	4002
D (nm)	0	22	42	74	75	80	99	101
ΔX (nm)	0	62.2	182	408	454	509	636	667
No.	9	10	11	12	13	14		
F (nN)	4039.2	3097.2	2719.2	2365.2	1357.2	0		
D (nm)	118.9	136	164	162	157	154		
ΔX (nm)	673.2	516.2	453.2	394.2	226.2	0		

REFERENCES

(1) Zhang, L.; Yang, T.; Du, C.; Liu, Q.; Tang, Y.; Zhao, J.; Wang, B.; Chen, T.; Sun, Y.; Jia, P.; Li, H.; Geng, L.; Chen, J.; Ye, H.; Wang, Z.; Li, Y.; Sun, H.; Li, X.; Dai, Q.; Tang, Y.; Peng, Q.; Shen, T.; Zhang, S.; Zhu, T.; Huang, J., Lithium Whisker Growth and Stress Generation in an in Situ Atomic Force Microscope–Environmental Transmission Electron Microscope Set-Up. *Nat. Nanotechnol.* **2020,** *15* (2), 94-98.

(2) Zhu, T.; Li, J., Ultra-Strength Materials. *Prog. Mater. Sci.* **2010,** *55* (7), 710-757.

(3) Richter, G.; Hillerich, K.; Gianola, D. S.; Mönig, R.; Kraft, O.; Volkert, C. A., Ultrahigh Strength Single Crystalline Nanowhiskers Grown by Physical Vapor Deposition. *Nano Lett.* **2009,** *9* (8), 3048-3052.

(4) Xu, C.; Ahmad, Z.; Aryanfar, A.; Viswanathan, V.; Greer, J. R., Enhanced Strength and Temperature Dependence of Mechanical Properties of Li at Small Scales and Its Implications for Li Metal Anodes. *Proc. Natl. Acad. Sci. U.S.A.* **2017,** *114* (1), 57-61.

(5) He, Y.; Ren, X.; Xu, Y.; Engelhard, M. H.; Li, X.; Xiao, J.; Liu, J.; Zhang, J.-G.; Xu, W.; Wang, C., Origin of Lithium Whisker Formation and Growth under Stress. *Nat. Nanotechnol.* **2019,** *14* (11), 1042-1047.

(6) Xiang, B.; Wang, L.; Liu, G.; Minor, A. M., Electromechanical Probing of Li/Li_2CO_3 core/Shell Particles in a TEM. *J. Electrochem. Soc.* **2013,** *160* (3), A415-A419.

(7) Fincher, C. D.; Ojeda, D.; Zhang, Y.; Pharr, G. M.; Pharr, M., Mechanical Properties of Metallic Lithium: From Nano to Bulk Scales. *Acta Mater.* **2020,** *186*, 215-222.

(8) Herbert, E. G.; Hackney, S. A.; Thole, V.; Dudney, N. J.; Phani, P. S., Nanoindentation of High-Purity Vapor Deposited Lithium Films: A Mechanistic Rationalization of Diffusion-Mediated Flow. *J. Mater. Res.* **2018,** *33* (10), 1347-1360.

(9) LePage, W. S.; Chen, Y.; Kazyak, E.; Chen, K.-H.; Sanchez, A. J.; Poli, A.; Arruda, E. M.; Thouless, M. D.; Dasgupta, N. P., Lithium Mechanics: Roles of Strain Rate and Temperature and Implications for Lithium Metal Batteries. *J. Electrochem. Soc.* **2019,** *166* (2), A89-A97.

(10) Masias, A.; Felten, N.; Garcia-Mendez, R.; Wolfenstine, J.; Sakamoto, J., Elastic, Plastic, and Creep Mechanical Properties of Lithium Metal. *J. Mater. Sci.* **2019,** *54* (3), 2585-2600.

(11) Sargent, P. M.; Ashby, M. F., Deformation Mechanism Maps for Alkali Metals. *Scripta Metall.* **1984,** *18* (2), 145-150.
(12) Porz, L.; Swamy, T.; Sheldon, B. W.; Rettenwander, D.; Frömling, T.; Thaman, H. L.; Berendts, S.; Uecker, R.; Carter, W. C.; Chiang, Y.-M., Mechanism of Lithium Metal Penetration through Inorganic Solid Electrolytes. *Adv. Energy Mater.* **2017,** *7* (20), 1701003.